Naval Information Warfare Center PACIFIC

TECHNICAL REPORT 3220
DECEMBER 2020

Plasmonic Retroreflectors for Passive Optical Identification

Burton H. Neuner III, Ph.D.
Brooke L. Myers
Wayne C. McGinnis, Ph.D.
David T. Wayne, Ph.D.
NIWC Pacific

Naval Information Warfare Center Pacific (NIWC Pacific)
San Diego, CA 92152-5001

This page is intentionally blank.

TECHNICAL REPORT 3220
DECEMBER 2020

Plasmonic Retroreflectors for Passive Optical Identification

Burton Neuner H. III, Ph.D.
Brooke L. Myers
Wayne C. McGinnis, Ph.D.
David T. Wayne, Ph.D.
NIWC Pacific

Administrative Notes:
This report was approved through the Release of Scientific and Technical Information (RSTI) process in January 2020, and formally published in the Defense Technical Information Center (DTIC) in December 2020.

NIWC Pacific
San Diego, CA 92152-5001

NIWC Pacific
San Diego, California 92152-5001

A. D. Gainer, CAPT, USN
Commanding Officer

W. R. Bonwit
Executive Director

ADMINISTRATIVE INFORMATION

The work described in this report was performed by the Advanced Photonic Technologies Branch of the Enterprise Communications and Networks Division, Naval Information Warfare Center Pacific (NIWC Pacific), San Diego, CA. Further assistance was provided by Atmospheric Propagation Branch, Communications Division. The NIWC Pacific Naval Innovative Science and Engineering (NISE) Program provided funding for this Basic Research project.

Released by
Brent Murray, Division Head
Enterprise Communications and Networks

Under authority of
Susie Hartzog, Department Head
Communications and Networks

Edited by:
Lisa Godinez

EXECUTIVE SUMMARY

This report presents the study of plasmonic retroreflecting devices for passive optical identification and tagging. Devices were designed to operate in the absence of electrical power and impart a unique spectral signature in relation to incoming light. The narrow-band, low-reflectivity response originates from the generation of surface plasmon-polaritons confined to thin metal films deposited on solid glass retroreflector prisms. The effect is highly dependent on film thickness, film type, prism type, and the incident angle of interrogating light. Numerical modeling on right angle prisms (RAPs) and corner cube retroreflectors (CCRs) demonstrated the desired plasmonic effect. Laboratory experiments on these devices validated the concept, but spectral bandwidths and magnitudes were marginal. Recommendations for future research and development are presented. Optimized plasmonic retroreflectors hold promise as passive optical identification and tagging devices for vehicles, shipping containers, transportation hardware, and other manufactured goods. Plasmonic retroreflector devices enable unique optical identification while avoiding the jamming and spectrum allocation issues more common to radio-frequency systems.

This page is intentionally blank.

CONTENTS

Figures

1. INTRODUCTION

Global inventories of vehicles, shipping containers, transportation hardware, and other manufactured devices continue to grow. The demands for passive (non-powered), inert (non-hazardous), and sensitive identification and tagging methods grow as well. Presently, devices are used for tagging an object at a standoff distance and subsequently interrogating the object, e.g., at a future time, whereby tracking is achieved for proper identification. The tag placed on the object emits a unique code or signature, thereby allowing the object to be identified among other objects. Such devices typically operate passively in the radio-frequency (RF) spectrum or operate by using electrical power for actively generating a unique RF signature. The RF spectrum remains vulnerable to jamming and spectrum allocation issues. A need exists for improving the identification process of objects at a standoff distance and for improving the power requirements.

Colored glass or interference-based optical filters could deliver unique spectral identification, but these devices typically exhibit shallow attenuation depths, wide bandwidths, minor dependencies on incident angle, or a combination thereof (Figure 1 (left)). Furthermore, they require an additional method to return the interrogating beam back to the observer.

This report presents the study of plasmonic retroreflecting devices for passive optical identification and tagging. Devices were designed to operate in the absence of electrical power and impart a unique spectral signature in relation to incoming light. The narrow-band, low-reflectivity response (Figure 1 (right)) originates from the generation of surface plasmon-polaritons confined to thin metal films deposited on solid glass retroreflector prisms. The effect is highly dependent on film thickness, film type, prism type, and the incident angle of interrogating light. Building on concepts detailed in United States Patent, “Retroreflective Optical System and Methods” [1], numerical modeling on right angle prisms (RAPs) and corner cube retroreflectors (CCRs) illustrated the plasmonic effect. Experimental research and development validated laboratory testing. This report presents the results of modeling and experimentation and provides recommendations for future theoretical and experimental studies.

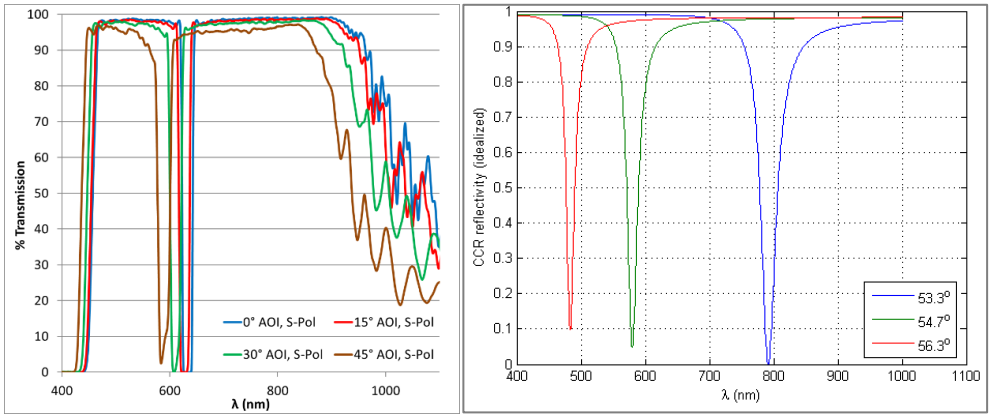

- Left: Example transmission plot of a notch filter with narrow bandwidth and low reflectivity but weak angular dependence (Thorlabs NF633-25).
- Right: Simplified illustration of the plasmonic retroreflector concept.

Figure 1. Thin metal films coating the rear faces of retroreflectors exhibit near-zero reflectivity with narrow bandwidth, and demonstrate strong spectral dependence on small incident angle changes. (Idealized numerical model)

This page is intentionally blank.

2. BACKGROUND

2.1 PLASMONICS

Surface plasmon-polaritons (SPPs) or surface phonon-polaritons are electromagnetic surface waves tightly confined to the interface between polaritonic ($\varepsilon < 0$) and dielectric ($\varepsilon > 0$) materials. Negative permittivity ε can result from (i) the collective oscillation of conduction electrons (plasmons) in metals such as gold (Au) and silver (Ag), or (ii) lattice vibrations (phonons) in polar crystals such as silicon carbide (SiC), zinc selenide (ZnSe), and indium phosphide (InP).

Surface plasmons are typically excited by visible-range and near-infrared-range photons, while surface phonons generally exist in the mid-infrared range. In both cases, the nature of the excitation is such that the incident light source alone is insufficient to excite the mode (i.e., the longitudinal wavevector is too small). Therefore, a coupling method is required. For the present study, we focus our attention on SPPs, and thus consider metal films and visible-band to near-IR-band incident light.

The SPP propagation wavenumber kSPP (which will be given below in Eq. 1) implies that $k_{SPP} > \omega/c$, where $\omega = 2\pi c/\lambda$, and λ is the vacuum wavelength of light. Since the SPP wavenumber is larger than that provided by incident radiation, auxiliary coupling methods such as gratings or high-index prisms are necessary to excite surface waves [2]. When a dielectric prism is used, either Otto configuration or Kretschmann configuration is employed. The Kretschmann case, which is relevant to this work, involves depositing metal directly on the prism: here, the evanescent electric field extends through the metal film and excites plasmons at the outer metal–air interface (or metal–film interface, if protective film coatings are used).

The dielectric permittivity ε describes how a material will respond to an incident electric field; matter with $\varepsilon > 0$ polarizes in the same direction as electric field vector E, whereas matter with $\varepsilon < 0$ polarizes in the opposite direction to E. Metals and polar crystals exhibit negative permittivity in certain frequency ranges; $\varepsilon < 0$ occurs in metals for frequencies below the plasma frequency. Free electron gas oscillation is responsible for the metal's "plasmonic" behavior. The coupling of photon radiation to a surface excitation is known as surface polariton generation. The unique excitation caused by the surface plasmon-polariton dispersion relation is possible at the interface between materials that possess dielectric permittivity of the opposite sign [2]. The field of plasmonics employs SPPs to accomplish many objectives, including high sensitivity detection of biochemical compounds, super-resolution imaging, and spectral filtering.

2.2 ELECTROMAGNETIC THEORY

Maxwell's equations provide a mathematical model for electric, optical, and radio technologies. They describe how electric and magnetic fields are generated, and, together with the Lorentz force law, they form the foundation of classical electromagnetism and classical optics. Solutions of Maxwell's equations are classified into S- and P-polarized modes, where the electric field E and the magnetic field H are parallel to the interface, respectively. Waves propagating along the interface must then possess a component of electric field that is perpendicular to the surface, so P polarization must be used.

The SPP wavevector dispersion relation can be presented in a simple, frequency-dependent form:

$$(1) \qquad k(\omega) = \frac{\omega}{c}\sqrt{\frac{\varepsilon_1 * \varepsilon_2(\omega)}{\varepsilon_1 + \varepsilon_2(\omega)}},$$

where

ε_1: dielectric layer, such as air or protective film, and

$\varepsilon_2(\omega)$: frequency-dependent polaritonic material, such as metal or crystal [2].

The permittivity of metallic gold, Au [3], is plotted in Figure 2. Surface plasmon-polaritons are supported when the permittivity is less than zero.

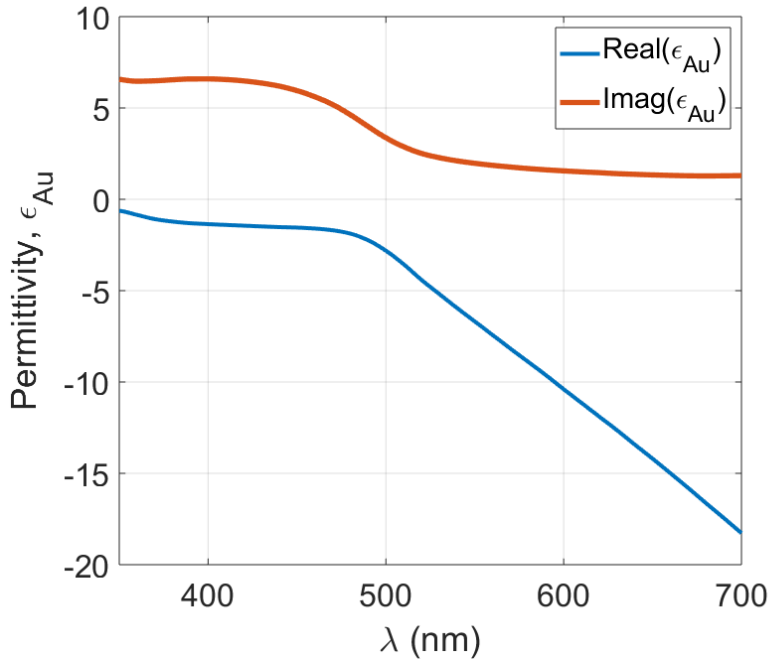

Figure 2. The permittivity of metallic gold, Au, is presented. Surface waves are supported when the real component of permittivity is less than zero.

Mode excitation requires wavevector matching by external methods such as prisms or gratings. A prism is used in this work, and the dielectric prism dispersion relation is

$$(2) \qquad k_x = \frac{\omega}{c}\sqrt{\varepsilon_{CCR}}\sin\theta,$$

where

k_x: describes the prism dispersion light line.

Efficient coupling to SPPs through the prism (which, in this case, is a RAP or CCR) occurs when kx ≈ Re (kSPP), and can be calculated by setting (Eq. 1) equal to (Eq. 2). The CCR dielectric

permittivity is εCCR, which is related to the index of refraction by εCCR=nCCR2, and the incidence angle inside the prism is the generalized θ.

When conditions are non-resonant (i.e., wavevectors are not matched), total internal reflection dominates, and near-unity light reflectivity is observed. But for specific wavelengths and incident angles that satisfy the equality described above, efficient polariton coupling occurs and is characterized by near-zero light reflectivity. Attenuated total reflection is central to the approach described in this report.

This page is intentionally blank.

3. NUMERICAL MODELING

3.1 RAY TRACING

With the principle of polariton excitation understood, we now consider ray tracing through the prism. The RAP model was less complex than the CCR model because the RAP can be represented in two dimensions. The model does not account for RAP height, but instead considers in the x–y plane refraction via Snell's law and specular reflection. The CCR model must account for reflections from its three sides, and in three dimensions. Beam propagation within the CCR is more complex, and is detailed below.

Figure 3 (left) shows a schematic of a CCR: three orthogonal reflecting planes. An incident ray is represented by a unit vector in three Cartesian coordinates,

$$\boldsymbol{n_i} = (n_{ix}, n_{iy}, n_{iz}), \tag{3}$$

where |ni|=1, and each plane reflection changes the sign of one of the coordinate components. The spherical coordinates φ_{in} (azimuth) and θ_{in} (elevation) are indicated in the schematic, which assist in the ray tracing process.

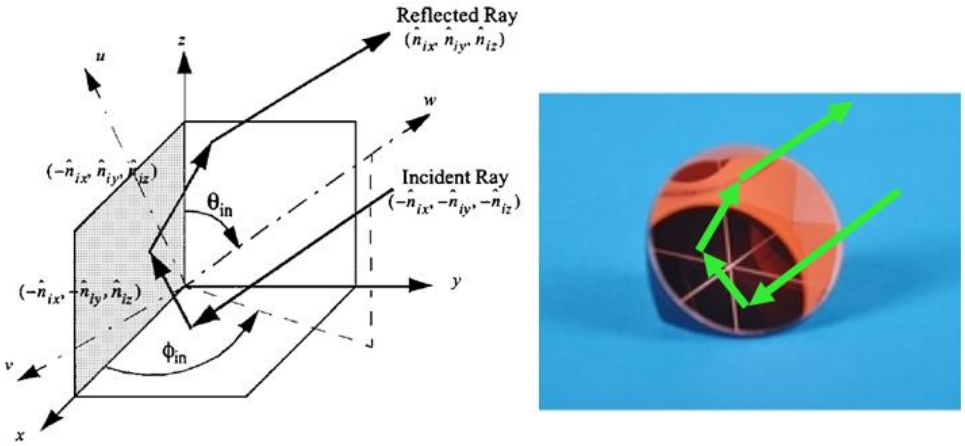

- Left: Ray tracing through the CCR. The spherical coordinates φin (azimuth) and θin (elevation) are indicated in the schematic.
- Right: Artist's conception of ray tracing through a glass CCR.

Figure 3. Ray tracing through a CCR.

If the azimuth and elevation angles are known, then the unit vector rays can be computed as follows:

$$\boldsymbol{n_i} = (\sin\theta_{in}\cos\varphi_{in}, \sin\theta_{in}\sin\varphi_{in}, \cos\theta_{in}). \tag{4}$$

As previously described, the angle of incidence upon a surface is critical to the excitation of surface waves, so we now compute the ray's angle of incidence upon each of the three interior CCR surfaces. We designate the x–y (bottom) plane as "A," which interacts with the first ray. We designate the x–z (side) plane as "B," which interacts with the second ray. We designate the y–z (rear) plane as "C," which interacts with the third ray. The fourth (final) ray is reflected back in the direction from which it originated, as depicted in Figure 3 (right). The incidence angle of an incoming ray upon a surface is defined as the inverse cosine of the ray's unit vector component normal to that surface. For example, the surface A is in the x–y plane, so the incidence angle of the first ray upon surface A is $\cos^{-1}(n_{iz})$. Presented together,

$$(\theta_A, \theta_B, \theta_C) = (\cos^{-1} n_{iz}\,, \cos^{-1} n_{iy}\,, \cos^{-1} n_{ix}). \quad (5)$$

Inside the CCR, the three incidence angles are now defined, and can be used in surface wave reflectivity calculations. However, one ray tracing issue remains: the incident ray will refract at the CCR's flat entrance face. Therefore, a three-dimensional vector calculation must be performed to trace the ray as it enters the CCR. The vector form of Snell's refraction law is presented as

$$\boldsymbol{s_2} = \frac{N_1}{N_2}[\boldsymbol{U} \times (-\boldsymbol{U} \times \boldsymbol{s_1})] - \boldsymbol{U}\sqrt{1 - \left(\frac{N_1}{N_2}\right)^2 (\boldsymbol{U} \times \boldsymbol{s_1}) \cdot (\boldsymbol{U} \times \boldsymbol{s_1})}, \quad (6)$$

where

s_2: refracted ray vector inside the CCR,

s_1: incident ray vector upon the CCR,

U: unit normal vector corresponding to the CCR face,

N_1: refractive index of the medium outside the CCR face (typically air, with N_1=1), and

N_2: refractive index of the solid CCR.

The creation of a CCR is often visualized by taking a perfect cube and cutting off one corner such that the lengths of the x, y, and z axes are equivalent. Such symmetry dictates that the unit vector normal to the face's surface is composed of three equal values. Therefore, the CCR's unit vector surface normal is

$$\boldsymbol{U} = \left(\frac{1}{\sqrt{3}}, \frac{1}{\sqrt{3}}, \frac{1}{\sqrt{3}}\right), \quad (7)$$

which, per Eq. 4, corresponds to an azimuth angle of φ_U=45˚ and an elevation angle of θ_U=54.7˚. Any rays incident at these angles would thus undergo no refraction. To understand the range of azimuth and elevation angles that are reasonably accessible to the CCR, Figure 4 displays an idealized net total angle (i.e., field of view half angle) of the incident ray from the CCR surface normal as a color map. As expected, an incident ray azimuth angle of φ=45˚ and elevation angle of θ=54.7˚ indeed yields a net angle of 0˚. Modestly negative values (down to -30˚) of azimuth and elevation are possible and yield effective CCR incident angles of 60˚ to 80˚.

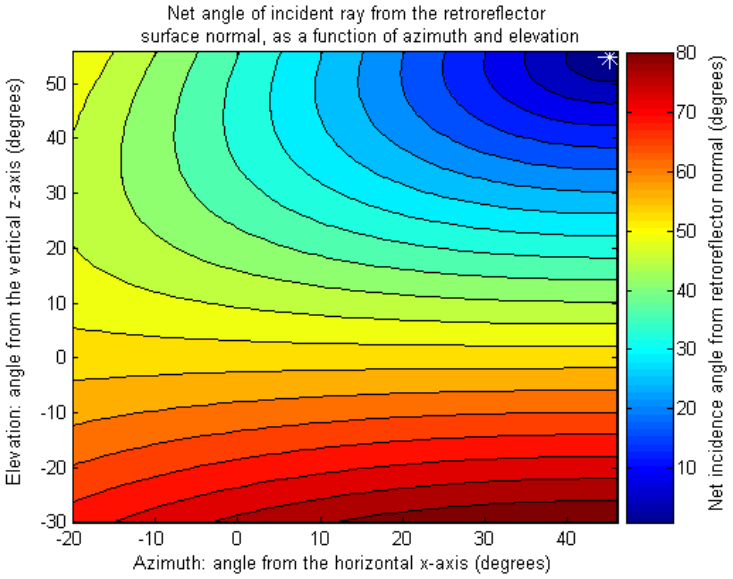

Figure 4. To understand the range of azimuth and elevation angles that are accessible to the CCR, the net total angle of the incident ray from the CCR surface normal is displayed as a color map.

3.2 REFLECTANCE MODELING SETUP

With an understanding of light rays incident upon the CCR and refraction at the CCR face, we proceed to the calculations of reflectance at the inner surfaces that support SPPs. Surface wave reflectance is solved using numerical calculations in MATLAB. The code solves Maxwell's equations in one dimension (longitudinal propagation) for S- and P- polarization. Figure 5 shows an idealized case: using purely P-polarized broadband illumination, a glass CCR with index 1.4, a 55-nm low-loss metal film deposited on each of the three reflection faces, a thick layer of protective dielectric film coating of index 1.1, an azimuth incident angle of 42˚, and an elevation incident angle of 54.7˚, we observe a net incidence ray angle of 2.4˚ from the CCR face, and three distinct reflection minima that correspond to SSP excitation at each of the three faces. The minima span the visible spectrum and correspond to three closely spaced but distinct angles incident upon the three cube faces.

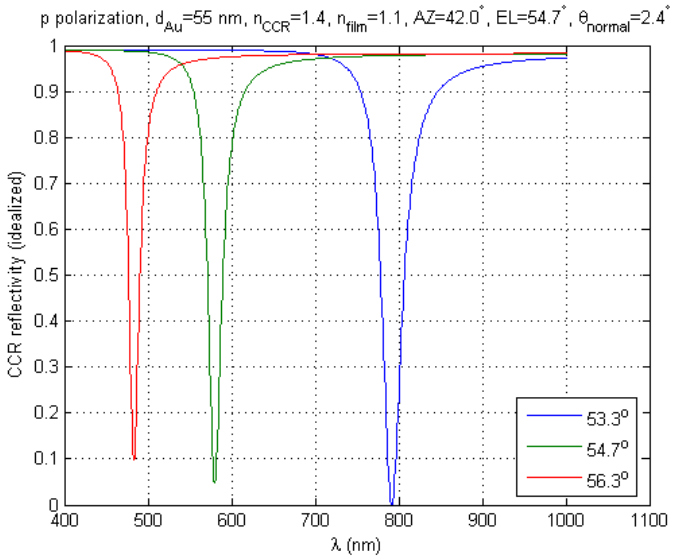

- In this idealized numerical model, thin metal films coating the rear faces of retroreflectors exhibit near-zero reflectivity with narrow bandwidth, and demonstrate strong spectral dependence on small incident angle changes. In this model, an idealized low-loss permittivity for gold is employed.

Figure 5. Simplified illustration of the plasmonic retroreflector concept.

In reality, it is not possible to have pure P polarization incident upon all three faces within the CCR; a realistic case would employ unpolarized light. Also, light is reflected from one cube face to another, so the resulting single spectrum consists of three unpolarized spectra multiplied together. Figure 6 shows the unpolarized spectrum (averaged S and P polarization) after three-face multiplication, which corresponds to the same parameters of Figure 5. Figure 7 and Figure 8 show two additional parameter sets; note that for Figure 8, the ray is incident normal to the CCR, resulting in a case where all reflections are symmetric and all three spectral minima are co-located.

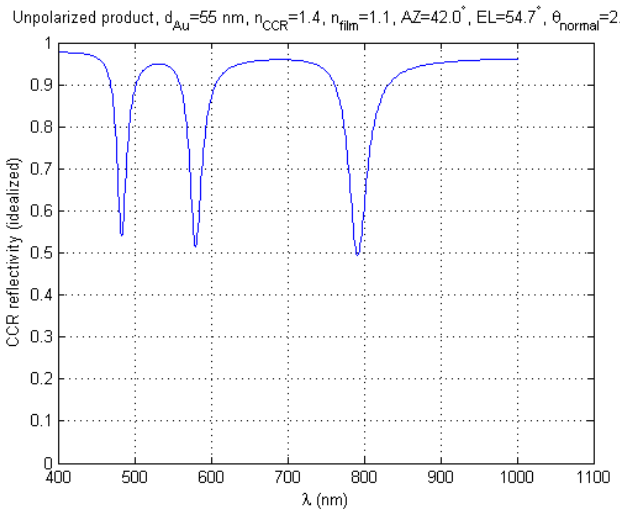

Figure 6. An unpolarized spectrum (averaged S and P polarization) after three-face multiplication is shown, corresponding to the same parameters of Figure 5.

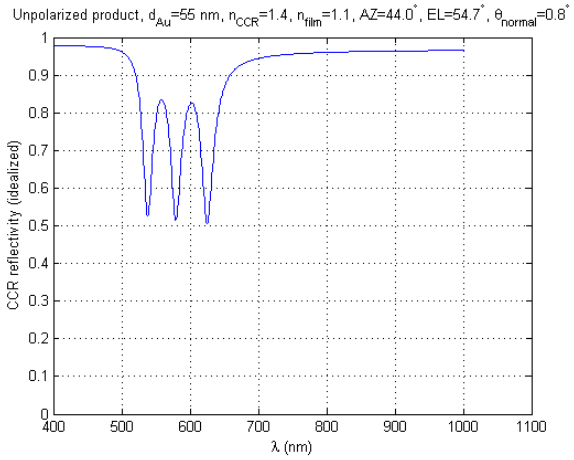

Figure 7. Additional parameter sets are shown.

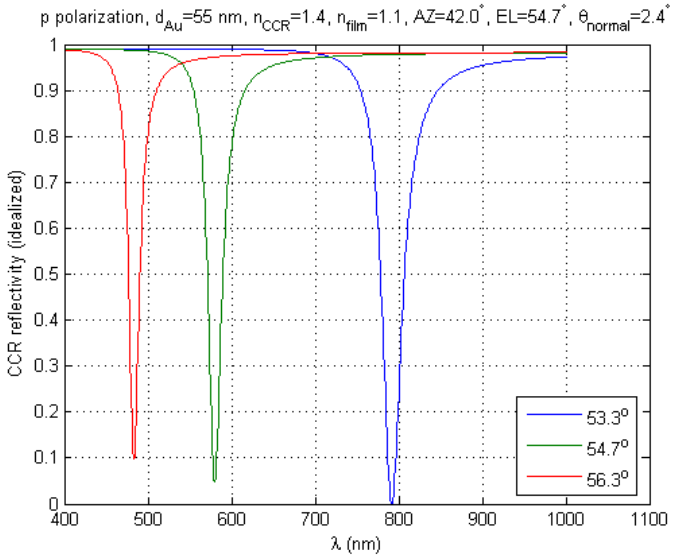

Figure 8. Corresponds to the case of an incident ray normal to the CCR, resulting symmetric reflections and all three spectral minima co-located.

It is clear from Figure 6, Figure 7, and Figure 8 that the metal-coated CCR's reflectivity spectrum is highly sensitive to incidence azimuth and elevation angles. Dramatic wavelength shifts occur with minute rotations, spreading from a single minimum at 580 nm when illuminated 0.0˚ from the face normal, to three minima spanning from 480 nm to 790 nm when illuminated just 2.4˚ off-axis.

This specific example shows the potential for spectroscopic tagging, identification, and orientation analysis, but numerous additional materials and parameters can be used for visible-band and near-IR-band applications. Variable parameters include (but are not limited to) the solid corner cube material (and thus the CCR index of refraction), the type and thickness of plasmonic metal film deposited on the three CCR reflecting faces, the choice to use or omit a protective dielectric overcoat on the metal (and if chosen, which material to select), and the input polarization desired (linear, elliptical, or unpolarized).

3.3 NUMERICAL MODELING OF EXPERIMENTAL DEVICES

The modeling of experimental devices began by enhancing the retroreflector models. Accurate dielectric permittivity functions, $\varepsilon(\lambda)$, for the gold metal film (Au) and glass prism (Corning N-BK7) were input into the models. The BK7 glass exhibits very low loss and chromatic dispersion, so a single value was employed ($\varepsilon_{BK7} = 2.3104$; $n_{BK7} = 1.52$). However, the realistic permittivity function for gold ($\varepsilon_{Au}(\lambda)$) exhibits substantial loss, so the function was updated with experimental data from a recent study [3] on gold films that possessed similar thicknesses (53 nm) to those used in this project (48 nm).

Numerical modeling incorporated the gold film thickness, the angle of incidence at the RAP or CCR entrance face, and the angle of incidence at the internal faces. Gold thickness was estimated at 48 nm by considering two independent measurements: thermal deposition sensors and laser transmission tests. In both simulations and experiments, P-polarized light generates the plasmonic-based attenuated total reflection effect, while S-polarized light does not.

3.3.1 RIGHT ANGLE PRISM MODELING

Starting with the 48-nm-thick gold film, we ran the RAP model. To explore the effect of thickness on the plasmonic response, we also modeled layers 20 nm thinner and thicker than 48 nm, as well as one ultra-thick layer tenfold greater (to approximate an infinitely thick, “mirror-like” film).

The results in Figure 9 are clear: the 48 nm-thick film is nearly ideal, exhibiting the desirably low reflection near 570 nm. The thin and thick films exhibit similar effects, but are either weaker in magnitude, undesirably wider in bandwidth, or both. The ultra-thick layer demonstrates no plasmonic effect at all and simply displays a “gold-mirror-like” reflection: the violet and blue bands are less reflective than the green and red bands, contributing to the characteristic gold tone. With the effect on thickness understood, we analyzed angular dependence.

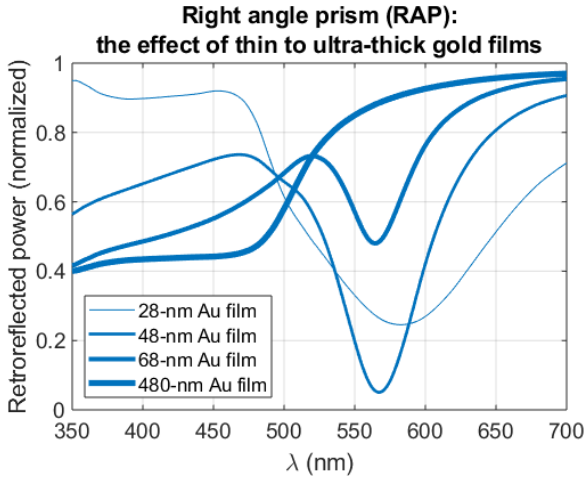

- The effect that gold thickness has on the desired plasmonic effect is pronounced. Films substantially thinner or thicker than 48 nm exhibit diminished attenuation.

Figure 9. Simulations on single-surface-coated RAPs are shown.

Modeling proceeded using a 48 nm-thick gold film, and was expanded to include angle of incidence (with respect to the prism's entrance face). To match experimental trials, angles of 0˚, 2˚, and 4˚ were initially planned. Results from the 4˚ model showed no effect and were difficult to interpret, so a third simulation was run at 3˚ instead to properly highlight the angular dependence. The results in Figure 10 show that the plasmonic peak is shifted to longer wavelengths (i.e., "red-shifted") as angle increases. (In both modeling and experimentation, larger incident angles correspond to smaller internal angles of incidence at the gold-coated surfaces.) Increased angle is even correlated with greater attenuated total reflection efficiency. With these promising results, we next explored CCR characteristics.

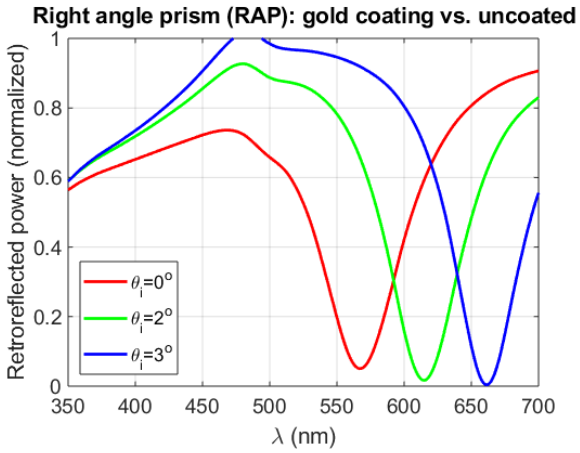

- P-polarized spectral data are normalized to S-polarized spectral data. RAP simulations on uncoated prisms result in 100% reflection, so the results in the right panel are appropriate for comparison to the experimental results above. Simulations at 4˚ yielded unclear results, so the 3˚ results are given instead to highlight the spectral shift with angle.

Figure 10. Simulations on the experimental device are shown.

3.3.2 CORNER CUBE RETROREFLECTOR MODELING

To explore the effect of thickness on the CCR's plasmonic response, we again modeled layers 20 nm thinner and thicker than 48 nm, as well as one ultra-thick layer (480 nm). The results in Figure 11 are less clear than those in Figure 9: the CCR's 28 nm-thick and 48 nm-thick films appear to indicate an effect at λ=480 nm, but the impact is minimal. Thicker films also approach the "gold-mirror-like" reflectivity observed in Figure 9, which is reassuring. Overall, this weak plasmonic effect dictates that film type and thickness must be further explored ahead of future CCR experiments.

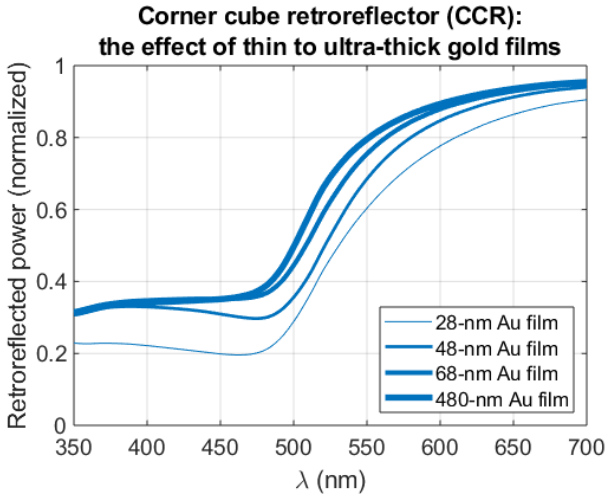

- The effect that gold thickness has on the desired plasmonic effect is minimal. Film type and thickness must be further explored ahead of future experimental fabrication.

Figure 11. Simulations on single-surface-coated CCRs are shown.

Despite the limited response observed above, we proceeded to model CCRs coated with gold on one surface and on all three surfaces. To match experimental trials, angles of 0˚ and 4˚ were simulated. Figure 12 presents our simulation results: angular differences are negligible, but the number of Au-coated surfaces strongly affects normalized reflectivity. Results from the experimental trials also showed minimal angular difference but pronounced reflectivity contrast between different devices. Comparisons will be detailed below in the Experimental Results section. As with RAP devices, future CCR devices must be judiciously designed to enable the desired plasmonic response.

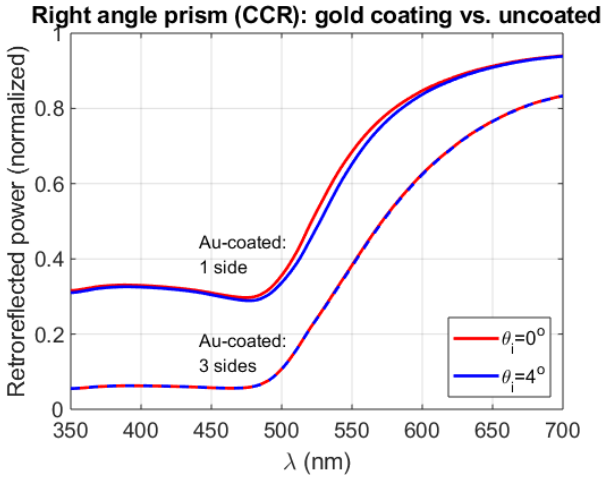

- The unpolarized spectra from coated CCRs are normalized to the spectra from the uncoated CCRs. Simulations indicate attenuation minima around λ=480 nm, but the effects are modest. Furthermore, the dependence on incident angle is negligible, suggesting the need for wider interrogation.

Figure 12. Simulations on the experimental device are shown.

4. DEVICE FABRICATION

To create the plasmonic retroreflector devices, gold was thermally evaporated onto glass prisms. This process is a type of physical vapor deposition in which the prism is secured within a high vacuum chamber and the solid metal material (gold) is cradled in an electrically heated boat. The boat melts and then vaporizes the deposition material. The increased temperature of the chamber creates a vapor pressure. This pressure raises the now vapor material so that it moves upward through the chamber, reaching the prism substrates that are placed above. The vapor evenly transports the material, resulting in a controlled and uniform film on the substrate.

4.1 DEPOSITION PROCEDURE

A heated-boat evaporator (Veeco VE-7700) was used to deposit gold (Au) films onto various optical surfaces of a retroreflector prism and a right-angle prism (Thorlabs PS975 and PS911, respectively; both are made of N-BK7 glass). Before depositing Au onto the prisms, a test deposition onto three borosilicate glass slides was performed. Two of the slides had previously been coated with a few hundred nanometers of titanium (Ti) using a Varian 980 RF diode sputtering system. The Ti deposition was done in anticipation of needing about 5 nm of Ti as an adhesion layer for subsequently deposited Au films. For all depositions, the bare prisms and glass slides were first cleaned by sequential rinsing with acetone, methanol, and deionized water, and then blown dry with argon gas. The optical surfaces to be coated were then gently swabbed with a methanol-soaked cotton swab and allowed to air dry. Fabrication for the RAPs began with three identical optics; each 25 mm tall with 25 mm X 25 mm square, rear faces. The entrance face was the diagonal hypotenuse of this “half cube,” and was 25 mm tall by 35 mm wide. The first RAP remained uncoated, the second RAP received deposition on one of the angled legs, and the third RAP received deposition on both of the angled legs. Fabrication on the CCR began with three identical CCRs; each with an entrance face of 25 mm diameter. The rear three faces comprise the “corner cube” and are mutually orthogonal. The first CCR remained uncoated, the second CCR received deposition on one of the angled faces, and the third CCR received deposition on all three of the angled faces. For the Au depositions, the items to be coated were placed over openings in a horizontal aluminum plate positioned approximately 30 cm above the evaporation boat. The prisms were fixed to the plate using optical mounts, as shown in Figure 13. Areas of the prisms that were not to be coated were covered with aluminum foil (secured with Kapton tape).

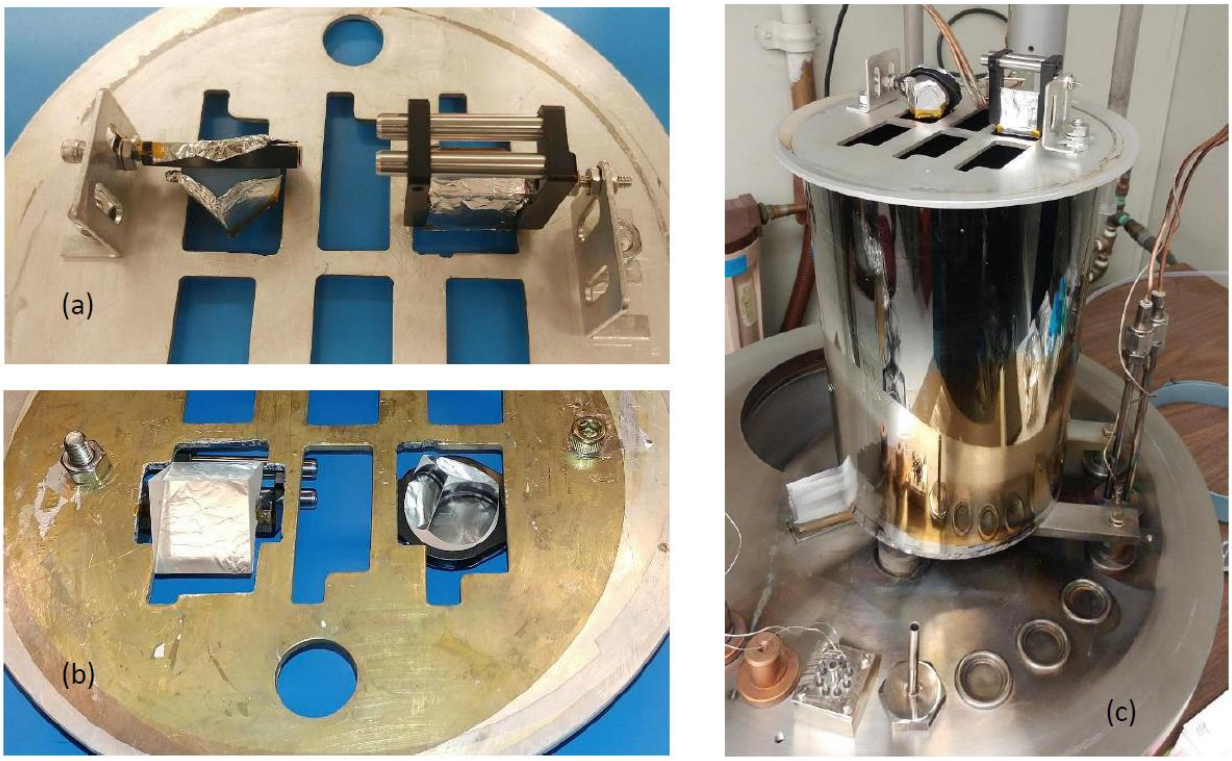

- (a) for coating of single faces of retroreflector prism (left) and right-angle prism (right);
- top view, (b) for coating of all optical surfaces of right-angle prism (left) and retroreflector prism (right);
- bottom view, and (c) placed on glass chimney as mounted in evaporator (with bell jar raised).

Figure 13. Prisms mounted on aluminum plate.

A tightly coiled 27.3-cm-long piece of 0.25-mm-diameter 99.9+% Au wire (weighing about 27.3 g) was placed in an alumina-coated tantalum evaporation boat. The evaporator bell jar was evacuated, using a mechanical pump, to a pressure of about 200 mtorr, and then pumped to below 10^{-5} torr using a diffusion pump (with a liquid-nitrogen-filled cold trap).

4.2 DEPOSITION RESULTS

Three depositions were performed using the following substrates: (i) three glass slides, (ii) one optical surface of each prism, and (iii) all optical surfaces of each prism. For each deposition, the procedure used is as follows. The evaporator current supply was set to the 300 Å range. The boat-heating current was slowly increased to 270 Å to 275 Å over the course of a couple of minutes. The Au deposition rate was monitored using a quartz crystal microbalance and an Inficon XTC thickness monitor (using evaporation parameters for Au determined from a previous Au deposition). The deposition rate, as reported by the thickness monitor, was roughly 3 Å/s for the first few minutes of the deposition (and steadily decreased thereafter as the Au in the boat was consumed). The total deposition time was between six and seven minutes.

In the first deposition, the evaporated gold adhered to all three glass slides, including the one with no Ti coating. Subsequent Au depositions onto the prisms were therefore done without first coating the prisms with Ti (i.e., the Au was deposited directly onto the glass surface of the prisms). The thickness of the Au deposited onto one of the Ti-coated slides was measured using a Dektak profilometer. Using optical analysis, it was determined the gold coating on the RAP and CCR was

approximately 48 nm thick. The surface profile for a scan across a corner of the Au film on a Ti-coated glass slide is shown in Figure 14.

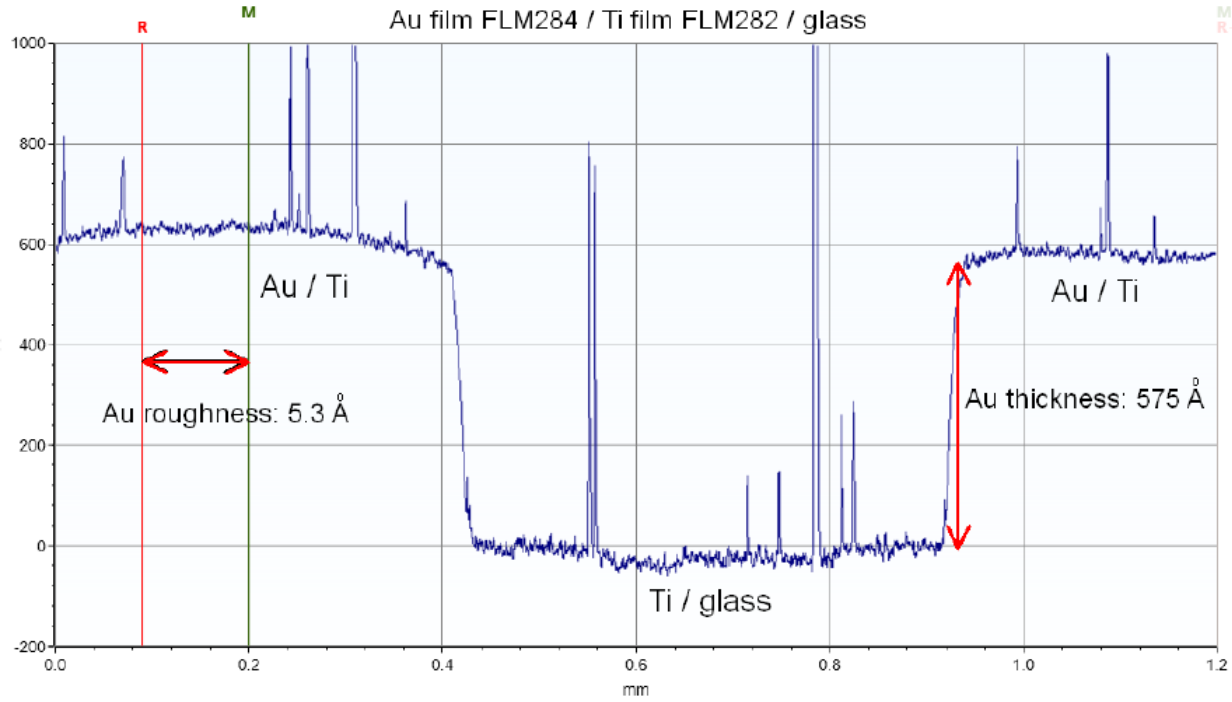

Figure 14. Dektak profile scan showing the thickness and roughness of the Au film deposited on a Ti-coated glass slide.

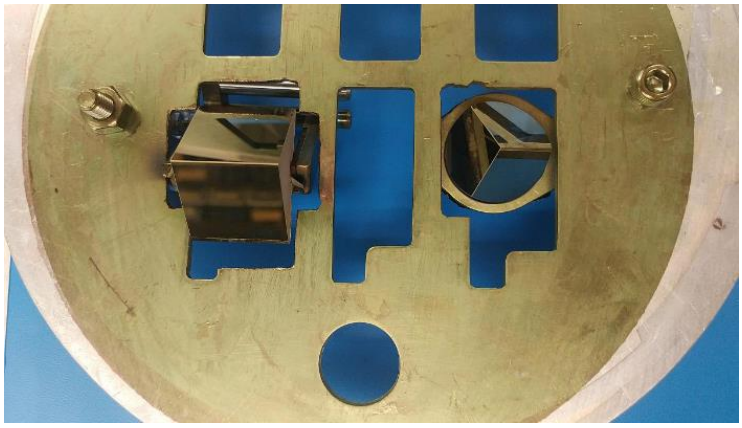

Figure 15. Gold films evaporated onto the reflection surfaces of the glass RAP and CCR.

This page is intentionally blank.

5. EXPERIMENTAL RESULTS

5.1 EXPERIMENTAL APPARATUS

RAP and CCR devices were illuminated with a Thorlabs broadband white-light source and analyzed with a Thorlabs Optical Spectrum Analyzer (OSA). Our experimental setup (Figure 16) did not allow for an absolute measurement of incident spectral power. Therefore, comparisons were made between P- and S- polarization on RAPs with and without gold films. When studying CCRs, unpolarized light interrogated the prisms, so comparisons were made between CCRs with and without gold films. For both devices, dependence on incident angle was studied.

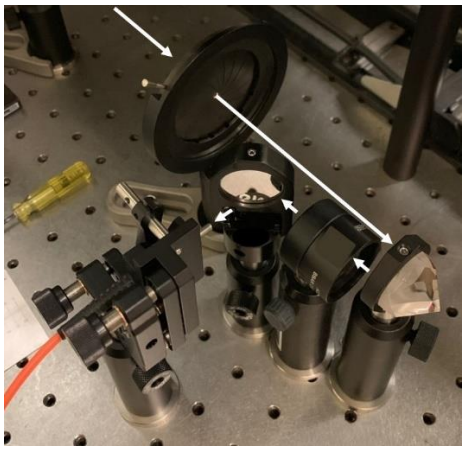

- The iris diameter defined the beam size.
- Light interrogated the device at the prism's right edge and retroreflected back at the prism's left edge.
- A 25 mm diameter, 50 mm focal length lens concentrated light to a ~1 mm spot.
- The turning mirror facilitated placement of the optical fiber (SMA905) and kinematic holder.
- Polarization optics and a precision rotation stage (both employed during RAP tests) are not shown in the figure.
- Also out of view is the broadband source (located in the upper left-hand corner).

Figure 16. The experimental setup is shown during CCR tests.

5.2 RIGHT ANGLE PRISM TESTING

In the first series of experiments, the uncoated, single-surface-coated, and dual surface coated RAPs were studied. We were not able to draw definitive conclusions from experiments on the third RAP with both surfaces coated. Therefore, we will focus this section on a comparison between the uncoated and single-surface-coated RAPs.

As reviewed, the method for normalization entailed rotating the incident polarization from P to S for each experiment, keeping all other parameters constant. In the left panel of Figure 17, results are given that compare the uncoated RAP to the single-surface-coated RAP. Each line corresponds to the given device at the angle of incidence shown in the legend, with P-polarized spectral data normalized to S-polarized spectral data. The uncoated RAP displays a relatively linear response, but the gold-coated RAP's minimum near λ=420 nm is pronounced. Here, the device coated with 48 nm gold displays preferential attenuation of P-polarized light, as predicted by electromagnetic models. To eliminate the influence from the prism itself or from any polarization biases in the OSA, the coated RAP plots were normalized to the uncoated RAP plots. In the right panel of Figure 17, results for three incident angles are given: P-polarized light that interrogates the gold-coated RAP displays clear, preferential attenuation in the violet-blue spectrum, indicative of surface plasmon-polariton

generation. Furthermore, when increasing the incident angle to 4˚, a small spectral lobe at λ=450 nm appears. Such features are expected as device orientation changes.

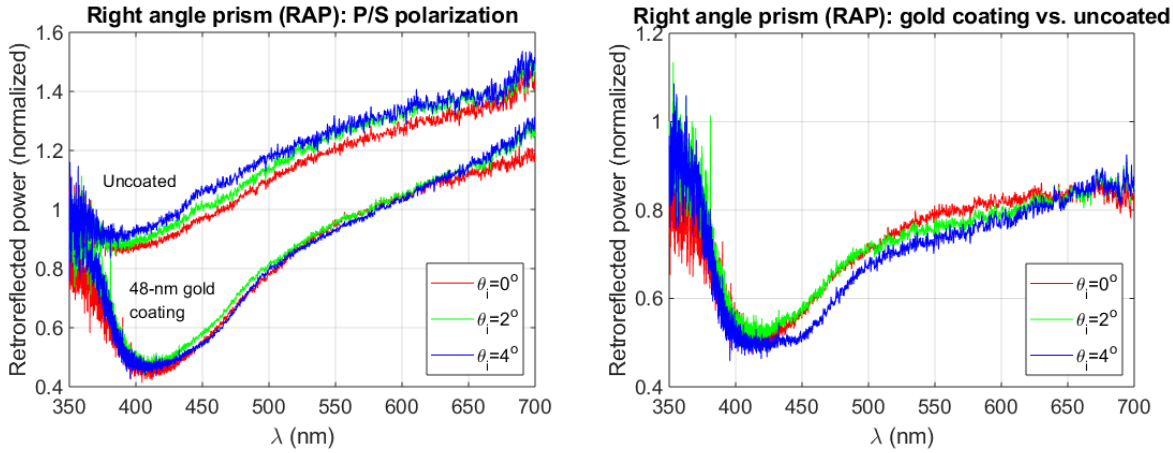

- Left panel: Reflection plots from the uncoated and single-surface-coated RAPs are shown. P-polarized spectra are normalized to S-polarized spectra.
- Right panel: Plots from the coated RAP were normalized to plots form the uncoated RAP to eliminate any polarization bias from the experimental setup.

Figure 17. P-polarized light that interrogates the gold-coated RAP displays preferential attenuation in the violet-blue spectrum, indicative of surface plasmon-polariton generation.

When comparing the simulations of Figure 10 to the experiments of Figure 17 (right panel), we observe two promising characteristics of the 48 nm-gold-coated RAP: (i) P-polarized light exhibits dramatic attenuation when compared to S-polarized light, and (ii) the effect appears dependent on incident angle. These two features indicate surface plasmon-polariton generation, and they give us the confidence to recommend further study on wavelength- and angle-sensitive optical retroreflecting devices. However, the observed magnitude, bandwidth, and spectral location of each feature are not fully understood using current models. All three characteristics are observed with lower qualities than predicted. Such discrepancies are expected in experimental systems, but future work must seek to understand the sources of disagreement and attempt to optimize these systems via improved modeling, fabrication, and testing.

5.3 CORNER CUBE RETROREFLECTOR TESTING

In the second series of experiments, multiple CCRs were studied. We focus this section on comparisons between (i) the uncoated and single-surface-coated CCRs and (ii) the uncoated and three-surface-coated CCRs.

Solid CCRs are known to convert linearly polarized input light into elliptically polarized light as radiation reflects from each of the three internal CCR faces [4]. Additionally, the polarization state evolves somewhat unpredictably. Therefore, unpolarized light was used to interrogate the CCR during experiments. As a result, normalization was performed by dividing plots from gold-coated CCRs by plots from uncoated CCRs. In an attempt to detect alignment sensitivity, two incident angles were studied: 0˚ and 4˚. Experiments shown in Figure 18 indicate attenuation minima around λ=480 nm; while the effects are modest, they agree with the simulations shown in Figure 12. A comparison of the two CCR devices (one-side coated and three-sides coated) highlights a pronounced

reflectivity difference, which is also observed in simulations. In the one-side coated CCR, the dependence on incident angle is visible at 4˚, suggesting the need for wider interrogation. For all experimental plots, signals at λ<400 nm are unreliable, resulting from weak lamp output and detector sensitivity. Overall, the agreement between CCR simulation and experiment is promising. Building on these results, we believe that improved CCR modeling, fabrication, and testing will results in optimized optical devices.

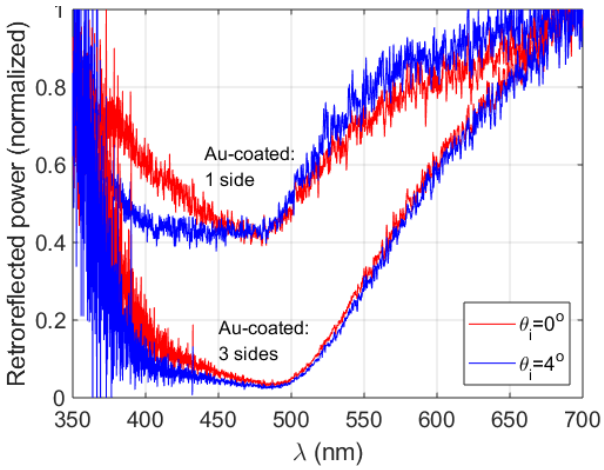

Figure 18. Reflection plots from CCRs coated on one side and on all three sides are shown. As input light was unpolarized, gold-coated CCR plots were normalized to uncoated CCR plots.

This page is intentionally blank.

6. RECOMMENDATIONS

The modeling and experimental results of this study indicate that the concept is indeed feasible. The devices remain relevant to current needs, but further study is required to accurately validate the principle. Multiple improvements to numerical modeling and experimental hardware are recommended.

6.1 NUMERICAL MODELING

The existing MATLAB code employs plane-wave propagation. Realistic propagation should be modeled using a range of input angles, as all light has a finite divergence/convergence angle. A series of calculations averaged over a range of angles would better approximate the experimental tests. The existing MATLAB code employs linearly polarized light. Two calculations were run (corresponding to P- and S- polarization), and the net effect was approximated via averaging.

An improved existing model or a new 2D or 3D model could better simulate the actual polarization properties directly. We recommend future model development in a finite element analysis program such as COMSOL Multiphysics or similar. These models could confirm the validity of existing code, or simply replace such code with its more capable toolset.

6.2 EXPERIMENTAL HARDWARE

To improve the accuracy of our study, the device fabrication and components used for laboratory analysis could be further developed. Improving the device fabrication would include adjustments to the prisms as well as the metal selection, deposition, and analysis. Upgrading the light source and components used for light detection would also provide improved laboratory analysis.

6.2.1 Device fabrication

Improving the device fabrication encompasses the prism selection as well as the choice of metal, deposition strategy, and analysis. The RAP and CCR prisms employed for this study were uncoated glass (N-BK7). Significant Fresnel reflections from the front surfaces were observed, complicating measurements. We recommend that future prisms are designed with visible-band antireflection coatings on the input faces (while leaving the angled prism surfaces uncoated for the metal deposition steps). The prism size (1”) and material (N-BK7) were sufficient for this study, but we recommend further investigation into new prism sizes and materials.

Low reflectivity and dampened plasmonic effects were likely caused by gold. This metal is non-toxic, non-oxidizing, and relatively easy to deposit. However, it exhibits poor reflection in the visible spectrum, and it attenuates and broadens the desired plasmonic effect. Future studies should employ a highly reflecting metal (such as silver). The plasmonic effect should be more pronounced, but the film will be susceptible to oxidation or corrosion over time.

Thermal deposition was sufficient for this study, but this technique may result in uneven film thicknesses and irregular grain boundaries. If future work discovers that smooth films of uniform thickness are required, then advanced methods (e.g., sputtering, atomic layer deposition) are recommended.

The present study explored RAPs with 0, 1, and 2 faces coated, and CCRs with 0, 1, or 3 faces coated with thin films. Unfortunately, analysis on the present devices with 2 or 3 faces coated was unclear at times. Nevertheless, such variations are critical to incremental analysis and understanding. We recommend that future studies include CCRs with 2 faces covered with thin films. We also

recommend that all variations be fabricated in two ways: thin metal films (~10s nm) and thick metal films (~10s μm). While thin films should display unique plasmonic effects, thick films should display typical “mirror-like” properties. A comparison of the two would thus eliminate effects that result from bulk-metal properties, such as the poor reflectivity observed in gold. With increased fabrication precision and improved metal selection, such incremental analysis may yield more insights. Metal thickness was determined in situ during deposition. While this method was sufficient for the present study, an independent measurement of smoothness and uniformity is recommended for all future work. Methods may include atomic force microscopy, profilometry, or ellipsometry.

6.2.2 Laboratory analysis

Additional components of the experimental hardware that could be improved upon are the light source and light detection apparatuses used in the laboratory analysis. The Thorlabs broadband white-light source employed for the present study was functional but limited in capability. It delivered modest optical power and was both highly divergent and non-uniformly polarized. The heated-coil filament caused these effects. The divergent beam was difficult to control and detect. A supercontinuum laser, for example, would deliver significant improvements in optical power, beam control, and polarization. We recommend an advanced light source.

The Thorlabs OSA detector was sufficient for this preliminary study, but we discovered that the OSA exhibits limited wavelength range and resolution. To ensure signal detection from the near-UV to the near-IR, we recommend an improved OSA. In addition, the OSA exhibits non-uniform detection of polarized light when placed directly in front of the optical device. The accompanying SMA optical fiber and cosine correcting diffuser were explored independently, and each served to increase uniformity. However, both had limitations. The optical fiber was difficult to align, and would require the purchase and installation of a fiber collimator to collect free-space light. The diffuser performed as expected, but only transmitted 0.1% to the OSA—a tiny fraction that made stable experiments impossible. If future experiments rely on this Thorlabs OSA, we recommend improvements to the fiber apparatus.

7. SUMMARY

Overall, this project provided promising initial results. With a thorough understanding of surface plasmon-polariton effects, models based on Maxwell's electromagnetic equations generated reflectance plots for multiple device configurations.

Numerical modeling incorporated the gold film thickness, the angle of incidence at the right angle prism (RAP) or corner cube retroreflector (CCR) entrance face, and the angle of incidence at each internal face. Two prism types—RAPs and CCRs—served as the foundations of the experimental devices. Thin gold films were thermally evaporated onto the prism surfaces. Laboratory testing employed broadband optical lamp illumination and optical spectrum analyzer detection. The resulting spectra displayed dependencies on the incident angle and input polarization.

As predicted, P polarization exhibited higher attenuation (i.e., lower reflectivity) than S polarization in certain bands—indicative of SPP generation. While the results of modeling and experimentation display qualitative agreement, the quantitative discrepancies remain.

Further work must be done to fully understand these spectra magnitude, bandwidth, and location inconsistencies. By improving numerical modeling, experimental hardware, device fabrication, and laboratory analysis, the measured plasmonic effects will be better understood. With such improvements, research on advanced versions of these plasmonic retroreflectors may pave the way toward practical applications in the near future.

This page is intentionally blank.

REFERENCES

1. Wayne, D. and Neuner, B., III [2020]: Retroreflective Optical System and Methods, US 10,598,592 B1, United States Patent and Trademark Office.
2. Raether, H. [1988] Springer-Verlag, Berlin, Germany: Surface plasmons on smooth and rough surfaces and on gratings, page 5, section 2.
3. Yakubovsky, D. I.; Arsenin, A. V.; Stebunov, Y. V.; Fedyanin, D. Yu.; Volkov, V. S. [2017]: Optical constants and structural properties of thin gold films, Opt. Express 25, 25574-25587.
4. Retroreflectors Lab Facts [2019]: Available at https://www.thorlabs.com/images/TabImages/Retroreflector_Lab.pdf. Accessed 9/26/2019.

This page is intentionally blank.

INITIAL DISTRIBUTION

84310	Technical Library and Archives	(1)
55360	B. Neuner III, Ph.D.	(1)
59150	B. Myers	(1)
71740	W. McGinnis, Ph.D.	(1)
55360	D. Wayne, Ph.D.	(1)
72110	D. Rees, Ph.D.	(1)

Defense Technical Information Center
Fort Belvoir, VA 22060–6218 (1)

This page is intentionally blank.

REPORT DOCUMENTATION PAGE

Form Approved
OMB No. 0704-01-0188

PLEASE DO NOT RETURN YOUR FORM TO THE ABOVE ADDRESS.

1. REPORT DATE *(DD-MM-YYYY)*	2. REPORT TYPE	3. DATES COVERED *(From - To)*
December 2020	Final	

4. TITLE AND SUBTITLE

Plasmonic Retroreflectors for Passive Optical Identification

5a. CONTRACT NUMBER

5b. GRANT NUMBER

5c. PROGRAM ELEMENT NUMBER

6. AUTHORS

Burton Neuner III, Ph.D.
Brooke Myers
Wayne McGinnis, Ph.D.
David Wayne, Ph.D.
NIWC Pacific

5d. PROJECT NUMBER

5e. TASK NUMBER

5f. WORK UNIT NUMBER

7. PERFORMING ORGANIZATION NAME(S) AND ADDRESS(ES)

NIWC Pacific
53560 Hull Street
San Diego, CA 92152–5001

8. PERFORMING ORGANIZATION REPORT NUMBER

TR-3220

9. SPONSORING/MONITORING AGENCY NAME(S) AND ADDRESS(ES)

Naval Innovative Science and Engineering, NIWC Pacific
53560 Hull Street
San Diego, CA 92152–5001

10. SPONSOR/MONITOR'S ACRONYM(S)

NISE

11. SPONSOR/MONITOR'S REPORT NUMBER(S)

12. DISTRIBUTION/AVAILABILITY STATEMENT

DISTRIBUTION STATEMENT A: Approved for public release. Distribution is unlimited.

13. SUPPLEMENTARY NOTES

14. ABSTRACT

This report presents the study of plasmonic retroreflecting devices for passive optical identification and tagging. Devices were designed to operate in the absence of electrical power and impart a unique spectral signature in relation to incoming light. The narrow-band, low-reflectivity response originates from the generation of surface plasmon-polaritons confined to thin metal films deposited on solid glass retroreflector prisms. The effect is highly dependent on film thickness, film type, prism type, and the incident angle of interrogating light. Numerical modeling on right angle prisms (RAPs) and corner cube retroreflectors (CCRs) demonstrated the desired plasmonic effect. Laboratory experiments on these devices validated the concept, but spectral bandwidths and magnitudes were marginal. Recommendations for future research and development are presented. Optimized plasmonic retroreflectors hold promise as passive optical identification and tagging devices for vehicles, shipping containers, transportation hardware, and other manufactured goods. Plasmonic retroreflector devices enable unique optical identification while avoiding the jamming and spectrum allocation issues more common to radio-frequency systems.

15. SUBJECT TERMS

plasmonics; electromagnetic; plasmonic retroreflector; passive optical identification; ray tracing; plasmon-polaritons; surface plasmon-polariton; SPP; surface phonon-polariton; right angle prism; RAP; corner cube retroreflector; CCR

16. SECURITY CLASSIFICATION OF:			17. LIMITATION OF ABSTRACT	18. NUMBER OF PAGES	19a. NAME OF RESPONSIBLE PERSON
a. REPORT	b. ABSTRACT	c. THIS PAGE			Burton Neuner, Ph.D.
U	U	U	SAR	42	19B. TELEPHONE NUMBER *(Include area code)* (619) 553-2885

This page is intentionally blank.

This page is intentionally blank.